ADVANCING EARTH AND SPACE SCIENCES

Geophysical Research Letters

RESEARCH LETTER
10.1029/2025GL115210

The Efficiency of Water Vapor on Top-of-Atmosphere Radiation

Jing Feng[1], **David Paynter**[2], **Nicole Feldl**[3], **Zhihong Tan**[1], **and Pu Lin**[2]

[1]Atmospheric and Oceanic Sciences Program, Princeton University, Princeton, NJ, USA, [2]Geophysical Fluid Dynamics Laboratory, Princeton, NJ, USA, [3]Earth and Planetary Sciences Department, The University of California, Santa Cruz, Santa Cruz, CA, USA

Key Points:

- The water vapor (WV) feedback cancels out a fraction of the temperature feedback with a nearly model-independent global mean efficiency $\epsilon \approx 0.46$
- The local radiative efficiency of WV varies substantially and is especially weak in polar regions
- This state-dependent efficiency can be explained by cloud masking effects and differences between surface and free-tropospheric temperatures

Supporting Information:

Supporting Information may be found in the online version of this article.

Correspondence to:

J. Feng,
jing.feng@Princeton.edu

Citation:

Feng, J., Paynter, D., Feldl, N., Tan, Z., & Lin, P. (2025). The efficiency of water vapor on top-of-atmosphere radiation. *Geophysical Research Letters*, *52*, e2025GL115210. https://doi.org/10.1029/2025GL115210

Received 7 FEB 2025
Accepted 30 JUL 2025

Author Contributions:

Conceptualization: Jing Feng
Formal analysis: Jing Feng
Investigation: Jing Feng
Methodology: Jing Feng, David Paynter
Software: Jing Feng
Supervision: David Paynter
Validation: Jing Feng
Visualization: Jing Feng
Writing – original draft: Jing Feng
Writing – review & editing: Jing Feng, David Paynter, Nicole Feldl, Zhihong Tan, Pu Lin

Abstract

Earth's climate sensitivity is greatly affected by the compensation between temperature feedback and water vapor (WV) feedback. Using abrupt 4xCO_2 experiments, we show that the global-mean WV feedback is nearly a linear function of the temperature feedback, the slope of which is explained by the longwave radiative efficiency of WV (ϵ). Although ϵ remains constant across models in the global mean, it exhibits substantial spatial variations and is particularly weak in Antarctica, where near-surface inversions decouple the surface from the free troposphere. We introduce a surface–free troposphere temperature difference (SFTD) metric, showing that positive SFTD (e.g., high lifting condensation level) amplifies ϵ, while negative SFTD (e.g., strong surface inversion) suppresses it. These findings provide a clear explanation of how local climate conditions modulate the radiative compensation between temperature and WV feedbacks.

Plain Language Summary

Earth's climate sensitivity depends strongly on how temperature and water vapor (WV) feedbacks compensate for each other to control the radiative energy loss to space. Here, we introduce a measure of this compensation, showing that the WV feedback is largely a function of the temperature feedback in different climate models. Although this relationship is robust on the global scale, it becomes sensitive to clouds, free-tropospheric lapse rate, and surface temperature in zonal mean climatology. In particular, the compensating effect is weak in high latitudes when near-surface temperature inversion occurs, highlighting the importance of base state climate in shaping Earth's climate response.

1. Introduction

Earth's climate is regulated by the balance between incoming shortwave radiation and outgoing longwave radiation (OLR) at the top of the atmosphere (TOA). Natural variations and anthropogenic emissions disrupt this balance by introducing radiative forcing (F), leading to an energy imbalance (N) at the TOA, which warms or cools the surface temperature until a new equilibrium is established. Radiative feedback parameters (λ) quantify changes per degree of global mean surface temperature increase (ΔT_s) under a given radiative forcing:

$$N = F + \lambda \, \Delta T_s. \tag{1}$$

As the surface warms, atmospheric and surface conditions evolve, further altering the global mean TOA radiative fluxes. The combined effect of these adjustments typically reduces the net energy imbalance, yielding a negative (stabilizing) value for λ. The temperature change ΔT_s required to restore energy equilibrium is often referred to as equilibrium climate sensitivity (Bony et al., 2013; Charney & DeVore, 1979).

It is well-known that the radiative feedback parameter is greatly contributed by temperature and water vapor (WV) feedback processes (Y. Huang et al., 2007). With surface warming, an increase in temperature enhances the thermal emission from the surface and atmosphere, reducing the energy imbalance and leading to a negative, stabilizing feedback process. An increase in specific humidity tends to reduce the thermal (longwave) emission of the atmosphere and absorb more shortwave radiation, leading to a positive, destabilizing feedback process. This compensation between temperature and WV feedbacks comes largely from a relatively constant global mean relative humidity (RH) in the atmosphere of the Earth (Held & Shell, 2012; Held & Soden, 2000; Ingram, 2010, 2013; Jeevanjee et al., 2021; Manabe & Wetherald, 1967; Soden & Held, 2006), so that the specific humidity is largely a function of temperature, controlled by the Clausius-Clapeyron relation. As a result, a negative feedback process caused by atmospheric warming is naturally linked with a positive feedback process caused by the related increase in specific humidity. This motivates studies to adopt a fixed RH feedback analysis framework (Held &

10.1029/2025GL115210

Shell, 2012; Zelinka et al., 2020) or combine WV and temperature (or lapse rate) feedback for feedback analysis (Shell et al., 2008; Sherwood et al., 2020; Soden et al., 2008). The combined temperature and lapse rate feedback has been found to effectively reduce the inter-model spread in global mean radiative feedback among climate models (Caldwell et al., 2016; Held & Shell, 2012), while leaving a distinct meridional structure that is more stabilizing in low latitudes and more destabilizing in high latitudes (Feldl & Merlis, 2023).

The strong temperature dependence of WV via the Clausius-Clapeyron relation is well-known, yet the quantitative relationship between temperature and WV remains unclear. This is in part because the radiative feedback is driven by a spatial integration over layer-by-layer atmospheric perturbations that have undergone complex radiative transfer processes. This study aims to achieve a quantitative explanation of the radiative compensation between temperature and WV.

2. Feedback Decomposition Methods

We derive radiative feedback parameters from 150-year abrupt-4xCO_2 experiments using 44 CMIP6 models. Specifically, we regress the first and last 10 years of global-mean, annual-mean downwelling radiative flux anomalies at the TOA against the global-mean, annual-mean near-surface air temperature, obtaining feedback parameters as the regression slopes. Radiative flux outputs in both all-sky and clear-sky (i.e., no clouds) conditions are used to separate the feedback parameters into longwave (LW) and shortwave (SW) components. In addition to the global-mean, zonal-mean radiative feedback is derived against the zonal-mean, annual-mean near-surface air temperature.

The LW and SW feedback parameters can be attributed to contributions from surface temperature (T_s), air temperature (T_a), WV, albedo (ALB), and clouds (CLD):

$$\lambda = \underbrace{\lambda_{T_s} + \lambda_{T_a} + \lambda_{LW,WV} + \lambda_{LW,CLD}}_{\lambda_{LW}} + \underbrace{\lambda_{SW,WV} + \lambda_{SW,CLD} + \lambda_{ALB}}_{\lambda_{SW}}, \tag{2}$$

Temperature (T_s and T_a) affects the longwave feedback, albedo affects the shortwave feedback, and atmospheric absorbers (WV and clouds) influence both. Methods such as partial radiative perturbation (PRP) (Wetherald & Manabe, 1988) and radiative kernels (Shell et al., 2008; Soden et al., 2008), introduced later in this section, are commonly used to estimate the magnitudes of each term.

Perturbations in these variables can be caused by various processes and can be combined to obtain the radiative feedback parameters of these feedback processes. For instance, the temperature feedback is often decomposed into a vertically uniform "Planck" (PL) feedback and a non-uniform "lapse rate" (LR) feedback process:

$$\lambda = \underbrace{\lambda_{T_s} + \lambda_{T_a}(\mathrm{PL})}_{\lambda_{\mathrm{PL}}} + \lambda_{\mathrm{LR}} + \underbrace{\lambda_{LW,WV} + \lambda_{SW,WV}}_{\lambda_{\mathrm{WV}}} + \underbrace{\lambda_{LW,CLD} + \lambda_{SW,CLD}}_{\lambda_{\mathrm{CLD}}} + \lambda_{\mathrm{ALB}}. \tag{3}$$

The Planck feedback (λ_{PL}) includes the direct contribution of surface warming, λ_{T_s}, and an atmospheric component under vertically uniform warming, $\lambda_{T_a}(\mathrm{PL})$. Consequently, the atmospheric warming term (λ_{T_a}) in Equation 2 is equivalent to $\lambda_{T_a}(\mathrm{PL} + \mathrm{LR})$, where PL and LR denote atmospheric warming processes, and $\lambda_{T_a}(\mathrm{LR})$ is equivalent to λ_{LR}.

λ_{WV} arises from enhanced longwave trapping and shortwave absorption due to the increased specific humidity associated with warming, as expressed in Equation 3. With this decomposition, λ_{LR} and λ_{WV} often exhibit strong anti-correlation and a large spread across models (Soden & Held, 2006; Soden et al., 2008), although adding them together reduces the overall spread by about half (Soden & Held, 2006).

Alternatively, Ingram (2010) and Held and Shell (2012) propose using RH as a state variable for feedback analysis, so that feedback processes due to atmospheric warming and moistening under fixed RH are combined. In this framework, Equations 2 and 3 can be rewritten as:

$$\lambda = \underbrace{\lambda_{T_s} + \lambda_{T_a}(\mathrm{PL}) + \lambda_{WV|RH}(\mathrm{PL})}_{PL^*} + \underbrace{\lambda_{LR} + \lambda_{WV|RH}(\mathrm{LR})}_{LR^*} + \lambda_{WV\nmid RH} + \lambda_{CLD} + \lambda_{ALB}, \tag{4}$$

10.1029/2025GL115210

where * denotes the sum of radiative feedback caused by warming and moistening under fixed RH. Here, $\lambda_{WV|RH}$ (both longwave and shortwave) is the portion of WV feedback that accompanies temperature changes at fixed RH, while $\lambda_{WV\nmid RH}$ corresponds to changes in RH itself. Held and Shell (2012) found that the inter-model spread in λ_{LR^*} is about half that in either λ_{LR} or λ_{WV}.

Regardless of whether one adopts the conventional (Equation 3) or the fixed RH framework (Equation 4), radiative feedbacks can be derived via either the radiative kernel method or the PRP method, using outputs from the same abrupt-4xCO_2 simulations, as described in Supporting Information S1. Following Smith et al. (2021), only changes between the surface and a time-varying tropopause (Reichler et al., 2003) are considered when calculating temperature and WV feedbacks.

3. The Radiative Efficiency of Water Vapor

Using the radiative kernel method, Figure 1a illustrates how different variables contribute to radiative feedbacks under both the conventional (Equation 3) and fixed-RH (Equation 4) frameworks. It shows that the longwave feedbacks from atmospheric temperature (λ_{T_a}) and WV following fixed-RH ($\lambda_{LW,WV|RH}$) compensate for each other, while the surface temperature feedback (λ_{T_s}) does not involve this compensation. To quantify this compensation, we define the "radiative efficiency of WV" as

$$\epsilon \equiv -\frac{\lambda_{LW,WV|RH}}{\lambda_{T_a}} \equiv 1 - \frac{\lambda_{LW,T_a^*}}{\lambda_{T_a}}, \tag{5}$$

where λ_{T_s}, $\lambda_{LW,WV\nmid RH}$, and $\lambda_{SW,WV}$ are excluded because they do not directly involve in this compensation. The term $\lambda_{LW,T_a}*$ is the longwave atmospheric feedback under fixed RH, equivalent to the sum of λ_{T_a} and $\lambda_{LW,WV|RH}$. Using multi-model mean values of $\lambda_{T_a} = -2.89$ W m^2 K^{-1} and $\lambda_{LW,T_a^*} = -1.57$ W m^2 K^{-1}, we obtain $\epsilon = 1 - 1.57/2.89 = 0.46$.

3.1. ϵ Explains the Well-Known Compensation Between Temperature and Water Vapor in Inter-model Spread

This compensation manifests not only in the multi-model mean but also across individual models. In Figure 1b, despite the substantial inter-model spread in λ_{T_a} and $\lambda_{LW,WV|RH}$ alone, their linear relationship (slope $= -\epsilon$) reveals a robust compensation. The near-zero intercept implies that $\lambda_{LW,WV|RH}$ has no independent component unrelated to temperature.

It is well-established that combining the lapse rate and WV feedbacks reduces inter-model spread, particularly under the specific humidity or fixed RH frameworks Soden and Held (2006) and Held and Shell (2012). To link ϵ with these studies more explicitly, we demonstrate that the inter-model spread in temperature feedback (Figure 1b, x-axis) is predominantly influenced by changes in the lapse rate (Figure 1c, x-axis):

$$\lambda_{T_a} \approx \lambda_{LR} + \bar{\lambda}_{T_a}(\text{PL}), \tag{6}$$

where $\bar{\lambda}_{T_a}(\text{PL}) = -2.47$ Wm^{-2}K^{-1} is the multi-model mean Planck feedback, which remains relatively uniform across models (Figure 1a) and is largely controlled by the magnitude of the temperature kernel.

The spread in WV feedback (Figure 1c, y-axis) primarily arises from the longwave component (Figure 1b, x-axis) as $\lambda_{SW,WV}$ exhibits small variation across models (0.02 W m^{-2} K^{-1}):

$$\lambda_{WV} \approx \lambda_{LW,WV|RH} + \lambda_{SW,WV}, \tag{7}$$

The variation in RH results in a nearly negligible global mean $\lambda_{LW,WV\nmid RH}$ (0.03 W m^{-2} K^{-1}), with an additional inter-model spread of 0.05 W m^{-2} K^{-1}, as shown on the y-axis of Figure 1c, in comparison with Figure 1b.

Combining the above, the global-mean WV feedback is approximately a linear function of λ_{LR}:

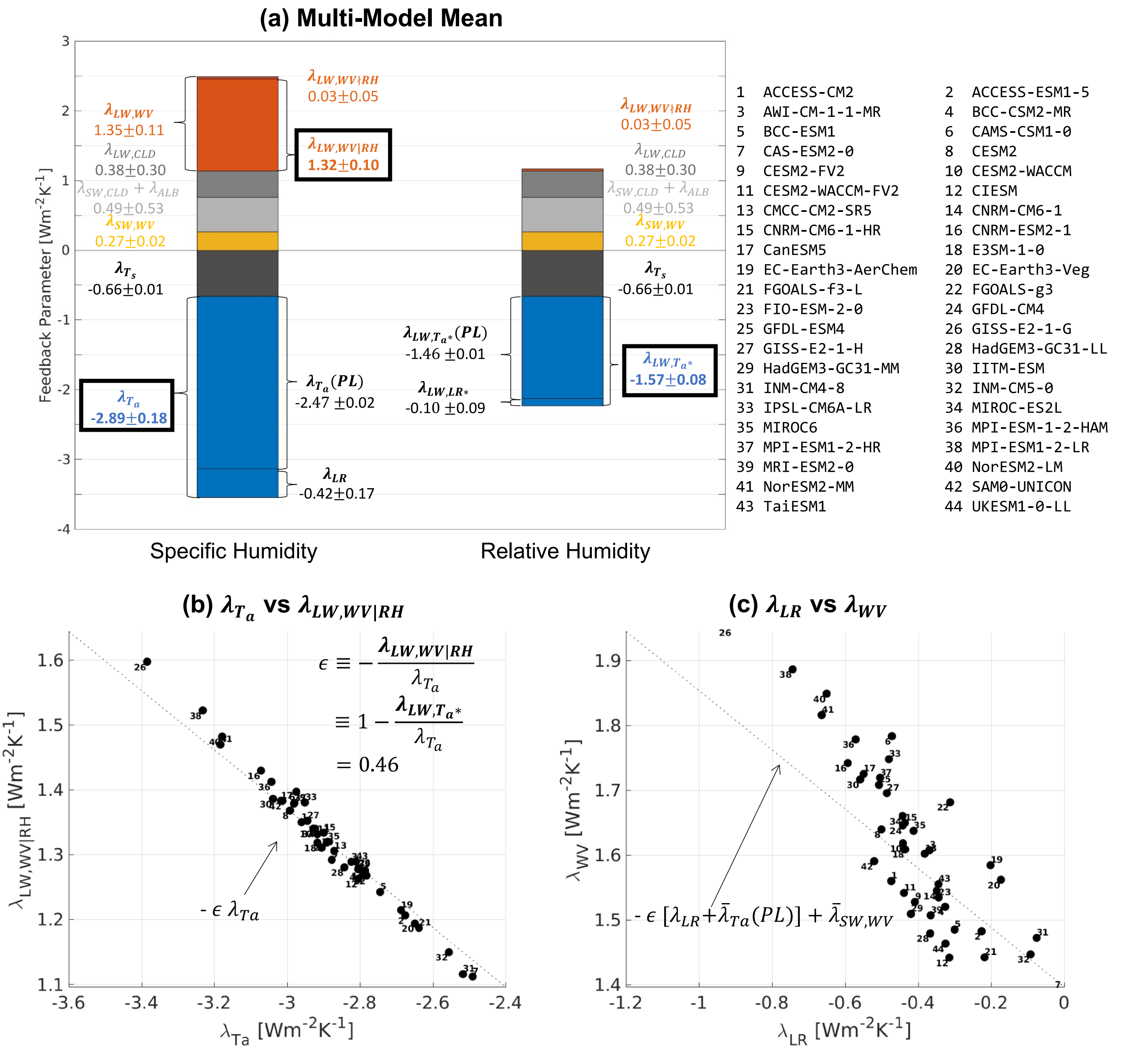

Figure 1. (a) Decomposing radiative feedback (W m^{-2} K^{-1}) of 150 years abrupt-4xCO_2 experiments using all-sky radiative kernel (Soden et al., 2008), following Zelinka et al. (2020) and the tropopause definition by Reichler et al. (2003). The mean and standard deviation of 44 CMIP6 models are marked. The mean of total radiative feedback is -1.03 W m^{-2} K^{-1}, with a standard deviation at 0.36 W m^{-2} K^{-1}. The total radiative feedback is decomposed following Equation 3 on the left and Equation 4 on the right. (b) The relation between atmospheric temperature feedback (λ_{T_a}, x-axis) and water vapor (WV) feedback holding fixed relative humidity ($\lambda_{LW,WV|RH}$) across 44 models. The efficiency of WV, ϵ, defined as the ratio between multi-model-mean λ_{Ta} and multi-model-mean $\lambda_{LW,WV|RH}$ (shown as a black dashed curve), is nearly fixed at 0.46 across all models. (c) Is the same as (b) except for the relation between lapse rate feedback (λ_{LR}, x-axis) and WV feedback ($\lambda_{WV} \equiv \lambda_{LW,WV|RH} + \lambda_{LW,WV\nmid RH} + \lambda_{SW,WV}$); the dotted line has the same slope at $\epsilon = 0.46$ but shifts -2.47 W m^{-2} K^{-1} in x-axis to remove the effect from $\bar{\lambda}_{T_a}(PL)$ and shifts 0.27 W m^{-2} K^{-1} in x-axis to add the effect from $\bar{\lambda}_{SW,WV}$.

$$\lambda_{WV} \approx -\epsilon\left[\lambda_{LR} + \bar{\lambda}_{T_a}(\mathrm{PL})\right] + \bar{\lambda}_{SW,WV}, \tag{8}$$

This relationship is illustrated by the dotted black line in Figure 1c and closely matches the slope shown in Figure 1b. With $\epsilon = 0.46$, the combined spread of $\lambda_{WV} + \lambda_{LR}$ is approximately half that of λ_{LR}, as noted by Soden et al. (2008), Shell et al. (2008), and Held and Shell (2012).

10.1029/2025GL115210

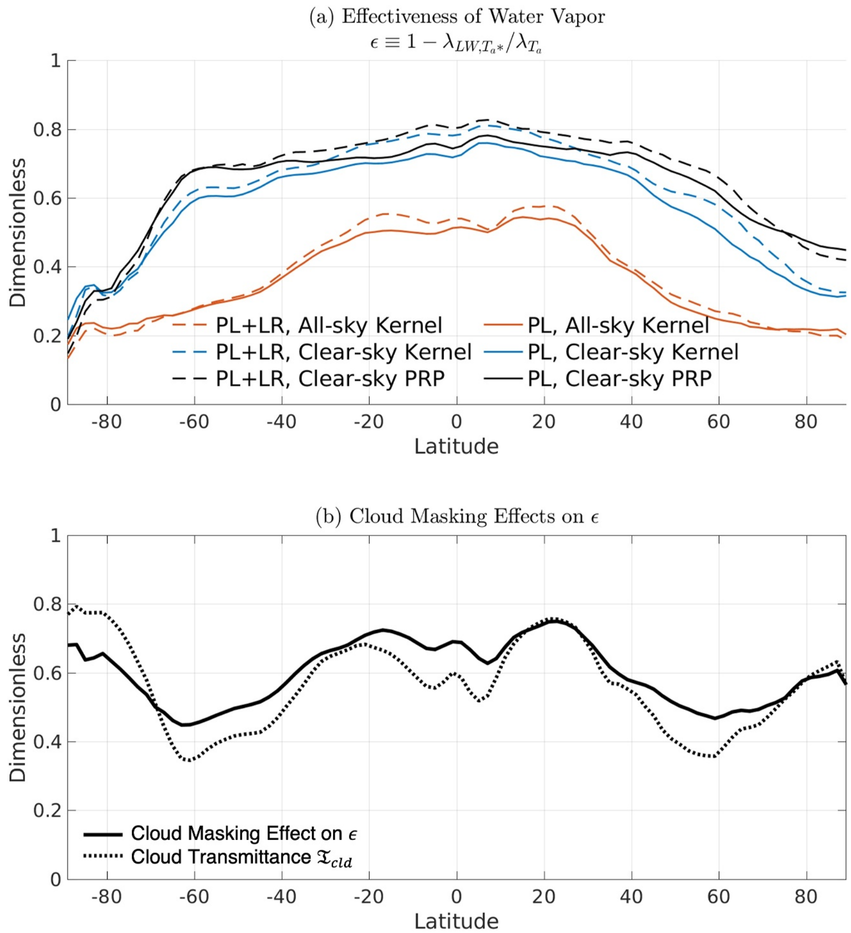

Figure 2. (a) Radiative efficiency of water vapor based on the all-sky radiative kernel (red), clear-sky radiative kernel (blue), and clear-sky partial radiative perturbation (black), using the abrupt 4xCO_2 simulation of CMIP6 models. The actual atmospheric warming ("PL + LR," dashed) and the vertically uniform atmospheric warming ("PL," solid) are applied. Results are inferred from radiative feedback parameters of multi-model-mean of the CMIP6 models presented in Figure S1 in Supporting Information S1. (b) Cloud masking effect, $\epsilon_{\text{all-sky}}/\epsilon_{\text{clear-sky}}$ (solid black, ratio between red and blue in panel (a)), compared to cloud transmittance $\mathfrak{T}_{\text{cld}}$ (dotted black).

In summary, global-mean WV feedback scales linearly with temperature feedback, governed by a consistent efficiency ϵ. This relation constrains the stabilizing feedback component of climate sensitivity across models (Figure 1a).

3.2. Understanding ϵ From Zonal-mean Decomposition

Under clear-sky conditions, accurate radiative calculations expect a radiative efficiency $\epsilon \sim 0.75$ (Feng, Paynter, Wang, & Menzel, 2023; Raghuraman et al., 2019), which is primarily governed by WV spectroscopy and pressure broadening (Feng, Paynter, & Menzel, 2023; Koll & Cronin, 2018; Koll et al., 2023). This value is significantly higher than the global-mean $\epsilon \approx 0.46$ inferred from all-sky kernels, but remains consistent when clear-sky kernels are used.

To understand this discrepancy, we decompose ϵ zonally. Figure 2a shows that the clear-sky ϵ peaks at approximately 0.8 in the tropics and decreases to 0.2 at high latitudes. This reveals a strong meridional structure, which is contrary to the uniform values expected from conceptual studies.

Clouds reduce ϵ by about 40% (solid black, Figure 2b), and this suppression closely tracks the broadband cloud transmittance:

$$\mathfrak{T}_{\text{cld}} = \frac{K_{T_s,\text{all-sky}}}{K_{T_s,\text{clear-sky}}},$$

where K_{T_s} denotes the surface temperature kernel. This ratio represents the extent to which clouds attenuate OLR (Shell et al., 2008; Soden et al., 2008). The zonal mean $\mathfrak{T}_{\text{cld}}$ (dotted black, Figure 2b) is approximately 0.6, exhibiting some latitudinal variability associated with the climatological distribution of clouds. The agreement between $\mathfrak{T}_{\text{cld}}$ and the reduction in ϵ confirms that cloud masking scales with longwave attenuation.

While clouds reduce ϵ overall, they do not account for the much weaker ϵ in high latitudes compared to the tropics. This dominance of temperature over WV feedback has long been recognized as an important characteristic of the polar climate (e.g., Langen et al., 2012; Pithan & Mauritsen, 2014; Taylor et al., 2013; Zelinka et al., 2012), and is further explained in Section 4.

4. Understanding the Sensitivity to Clear-Sky Base State

As ϵ evaluates the radiative efficiency of WV relative to temperature within a fixed RH framework, the differences in clear-sky ϵ between high latitudes and the tropics could arise from the lapse rate feedback process, surface warming patterns, or the base state conditions of the surface and atmosphere (on which the feedback processes occur). We first examine the role of lapse rate feedback processes, which are known to vary with latitude. However, as shown in Figure 2a, incorporating λ_{LR} only shifts ϵ by less than 0.1. It suggests that the differences in lapse rate changes are not the dominant driver of ϵ.

These findings indicate that clear-sky base-state conditions serve as a significant control on meridional variations in ϵ, which motivates further analysis using a method that does not depend on a fixed reference climate state. The PRP method (Wetherald & Manabe, 1988), unlike the radiative kernel approach, allows the base state to vary across different geographic locations and models. Global-scale PRP calculations (Supporting Information S1) are conducted for the same set of CMIP6 models, which are utilized to infer the clear-sky feedback parameters presented in Figure S1 in Supporting Information S1. Feedback parameters based on the PRP are similar to those based on the clear-sky kernel, but exhibit a much larger inter-model spread because the base state at each location is no longer prescribed. The PRP accounts for variations in climatological state across models, although it may be less accurate than the kernel for shortwave components in regions where diurnal variations are important, as the kernel data set is computed as the monthly mean of 3-hourly radiative sensitivity. In general, the monthly mean PRP method shows better agreement with the CMIP6 outputs compared to the clear-sky kernel (Figures S1g and S1h in Supporting Information S1). The inferred ϵ is shown as black in Figure 2a.

The PRP framework explicitly incorporates base state inputs, including surface temperature, atmospheric temperature, WV, and other greenhouse gas concentrations, allowing us to examine which of these shape the zonal structure of ϵ. Given that CO_2 and other well-mixed gases, along with stratospheric temperatures, are relatively uniform across latitudes, we focus on three key factors that exhibit strong meridional gradients: surface temperature, tropospheric temperature, and WV.

To isolate their roles, we perform mechanism-denial PRP experiments. Each experiment modifies one of the three base state components, using a "Control" state constructed from zonal, multi-model, and monthly means of the first 10 years of the abrupt-4xCO_2 runs (black lines in Figures 3c–3h). For each experiment, three radiative transfer calculations are performed:

1. The base state temperature, humidity, and surface conditions.
2. A 1-K uniform troposphere–surface warming with fixed specific humidity (compared with (1) to derive λ_{T_a}).
3. A 1-K uniform warming with fixed RH (compared with (2) to derive $\lambda_{LW,WV|RH}$).

In all experiments, the stratosphere is isothermal with uniform specific humidity. Tropopause temperature (T_t), pressure (P_t), and surface pressure (P_s) match the Control. Under these assumptions, the Control (black curve in Figures 3a and 3b) closely reproduces the multi-model-mean ϵ (solid black curve in Figure 2a), confirming that variations in ϵ are driven by base state structure, not meridional differences in warming.

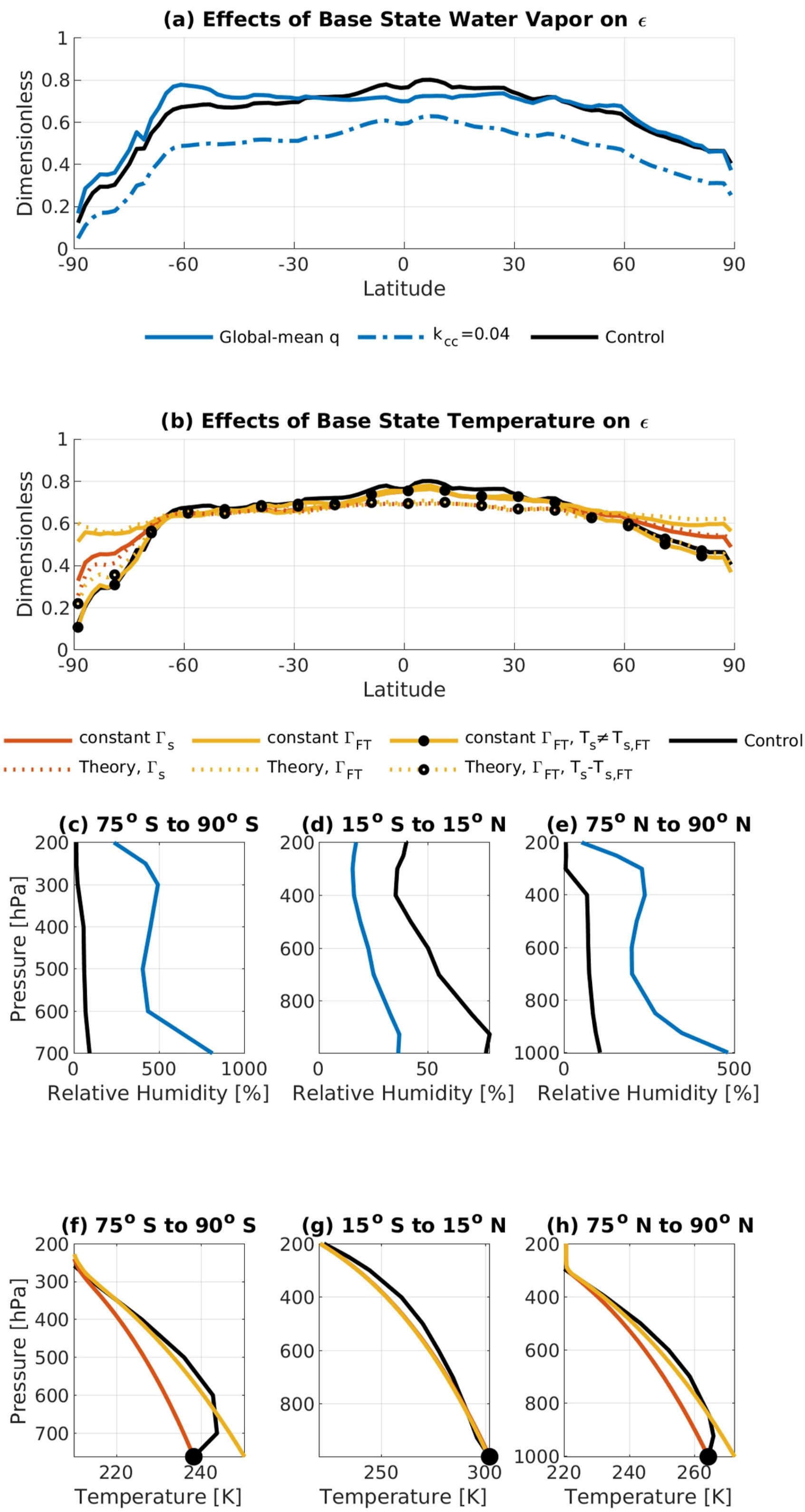
(a) Effects of Base State Water Vapor on ϵ
Dimensionless
Latitude
Global-mean q
k_cc=0.04
Control
(b) Effects of Base State Temperature on ϵ
Dimensionless
Latitude
constant Γ_s
constant Γ_FT
constant Γ_FT, T_s≠T_s,FT
Control
Theory, Γ_s
Theory, Γ_FT
Theory, Γ_FT, T_s-T_s,FT
(c) 75° S to 90° S
(d) 15° S to 15° N
(e) 75° N to 90° N
Pressure [hPa]
Relative Humidity [%]
(f) 75° S to 90° S
(g) 15° S to 15° N
(h) 75° N to 90° N
Temperature [K]

Figure 3.

4.1. Effects of Base State Water Vapor

Following PRP methods and the experiment set up described earlier, a "global mean q" experiment is designed to test whether the weak effect of WV at high latitudes is attributable to the low moisture content. This experiment assumes that all model grids share the same specific humidity profiles at the global mean values, leading to unrealistically high RH in high latitudes and low RH in the tropics, as presented in Figures 3c–3e. These inferred RH profiles at the altered base state are held fixed to compute the magnitude of $\lambda_{WV|RH}$ and ϵ. With the same global mean humidity, the magnitude of λ_{T_a} becomes more stabilizing at high latitudes and less stabilizing in the low latitudes compared to the Control (Figure S2a in Supporting Information S1). However, the resulting ϵ, displayed as the blue curve in Figure 3a, retains a meridional structure similar to that of the Control. As a result, λ_{T_a} is still much more important than $\lambda_{LW,WV|RH}$ in high latitudes, even though the moisture content is 10 times higher than the reality. This experiment suggests that the low moisture content cannot explain the weak ϵ in high latitudes.

We find that WV affects ϵ mainly through the Clausius-Clapeyron (CC) relationship, which describes how moisture content increases with warming. This relationship can be approximated as:

$$e \propto RHe^{k_{cc}\left(T-T_{\text{freeze}}\right)} \tag{9}$$

where e is the vapor pressure, T_{freeze} is 273.15 K, $k_{cc} \approx 0.07\ \text{K}^{-1}$, as in the August-Roche-Magnus formulation (Alduchov & Eskridge, 1996). The parameter k_{cc} characterizes the exponential sensitivity of vapor pressure to temperature, corresponding to roughly a 7% increase in saturation vapor pressure per 1 K of warming.

To isolate the role of this scaling term, we conduct a sensitivity experiment that reduces k_{cc} from 0.07 to 0.04 K^{-1}. A smaller k_{cc} weakens the increase in vapor pressure with warming, resulting in reduced ϵ (Figure 3a, blue dashed curve). This diminished ϵ makes the longwave feedback more stabilizing: the sum of $\lambda_{LW,WV|RH}$ and λ_{Ta} becomes more negative than in the Control experiment (Figure S2a in Supporting Information S1). In the extreme case where $k_{cc} = 0$, vapor pressure becomes constant and independent of temperature. Without additional WV from warming, there is no increase in atmospheric opacity, and thus zero ϵ.

These results show that the magnitude of ϵ is strongly controlled by the CC scaling but relatively insensitive to the absolute base-state moisture content. Therefore, under the real-world CC relation ($k_{cc} \approx 0.07\ \text{K}^{-1}$), the zonal-mean WV feedback is primarily shaped by the zonal-mean base state of temperature and temperature feedback.

4.2. Effects of Base State Temperature

To isolate the base state effects of the lower tropospheric temperature, surface temperature, and free tropospheric (FT) lapse rate, three experiments are conducted following the description at the beginning of Section 4.

In the first experiment, we retain the climatological surface temperature (T_s) but assume that the temperature lapse rate is uniform from the tropopause to the surface at Γ_s. This assumption constructs the temperature profiles as shown in Figures 3f–3h. The constant lapse rate at Γ_s generates a weaker meridional structure in ϵ, as shown in Figure 3b. It indicates that ϵ is weaker in high latitudes in part due to the weaker thermal contrast and the lapse rate between tropopause and surface. However, the constant lapse rate cannot fully explain the particularly weak ϵ over the Antarctic (75–90°S), likely due to the presence of near-surface inversion (Figures 3f and 3h).

Figure 3. Zonal mean water vapor (WV) efficiency (ϵ) calculated using the partial radiative perturbation method and an analytical theory under clear-sky conditions, highlighting effects of (a) base state of WV and (b) base state of air and surface temperature. Black curves in both panels are Control experiments, using temperature and humidity conditions of monthly mean, multi-model-mean of CMIP6 abrupt 4xCO_2 experiments (black in panels (c–h)). In panel (a), the control temperature profiles are applied to all cases. "global mean q" takes a global mean specific humidity profile (the relative humidity [RH] of which is shown as solid blue in panels (c–e)). "$k_{cc} = 0.04$" adopts the actual RH profile (black in panels (f–h)) but hypothetically assumes a weaker CC scaling. In panel (b), the control RH profile is applied to all cases. "Constant Γ_s" adopts idealized temperature profiles with vertically constant lapse rate, Γ_s, that maintains the climatological tropopause pressure, tropopause temperature, surface pressure, and surface temperature (red in panels (f–h)). "Constant Γ_{FT}" adopts a Γ_{FT} that maintains the maximum tropopause temperature and its pressure level; the Γ_{FT} and surface pressure are used to infer $T_{s,FT}$ as the surface temperature. The yellow curves with markers are the same as "Constant Γ_{FT}" except that the actual climatological surface temperature, as shown as black markers panels (f–h), is applied to replace $T_{s,FT}$. Dotted curves in panel (b) are estimates of ϵ estimated from Equation 11.

The second experiment is designed to examine the effects of lower tropospheric and surface temperatures. At each latitude, we construct a set of base state temperature profiles where the lower tropospheric temperature variation is removed, using a uniform FT lapse rate Γ_{FT}. The bottom of the FT layer is identified as the layer with the maximum FT temperature T_{FT}^m above 850 hPa. The 850 hPa is used because the emission of WV is most important in the layers above it (Feng, Paynter, Wang, & Menzel, 2023). The pressure and altitude at this layer are denoted as p_{FT}^m and z_{FT}^m, respectively. With the ideal gas law and hydrostatic balance, tropopause and surface pressure can be expressed as a function of temperature as (Wallace & Hobbs, 2006):

$$P_t = P_{FT}^m \left(\frac{T_t}{T_{FT}^m}\right)^{\frac{g}{R\Gamma_{FT}}}$$

where g is gravity (9.8 m s^{-2}), R is the specific gas constant for dry air (287.05 J kg^{-1} K^{-1}). This equation assumes that the temperature lapse rate is constant from the tropopause to the surface temperature. With this assumption, we can approximate the average FT lapse rate, Γ_{FT} as:

$$\Gamma_{FT} = \frac{g}{R}\frac{\ln\frac{T_t}{T_{FT}^m}}{\ln\frac{P_t}{P_{FT}^m}}$$

Assuming the FT lapse rate is further extended to the surface, the surface temperature $T_{s,FT}$ would be:

$$T_{s,FT} = T_t\left(\frac{P_s}{P_t}\right)^{\frac{R\Gamma_{FT}}{g}} = T_{FT}^m + z_{FT}^m\Gamma_{FT} \tag{10}$$

The constructed temperature profiles are shown as yellow in Figure 3; they overlap nicely with the Control in the middle and upper troposphere but omit the lower troposphere inversion. Using the idealized temperature profiles and surface temperature at $T_{s,FT}$ as the base state, the meridional differences in ϵ are greatly reduced (solid yellow curve without markers in Figure 3a). Compared to the first experiment, a higher lapse rate Γ_{FT} in place of Γ_s significantly enhances ϵ at high latitudes. It confirms that ϵ is proportional to the tropospheric lapse rate. Because the zonal mean Γ_{FT} is relatively constant (5.0–6.7 K km^{-1}) as the static stability of extratropics tends to be greater than a moist adiabat (Schneider & O'Gorman, 2008), ϵ produced by the Γ_{FT} experiment varies little with latitude.

The third experiment isolates the effects of lower tropospheric temperature variation and surface temperature. This experiment is identical to "Constant Γ_{FT}," except that the Control surface temperature is used in radiative transfer, instead of $T_{s,FT}$. As shown in Figure 3 (yellow curve with markers), this experiment overlaps with ϵ of Control, reproducing a weak ϵ in Antarctica despite its lack of atmospheric temperature inversion except just above the surface. The finding that the lower tropospheric temperature has almost no effect on ϵ is consistent with previous studies (Feng, Paynter, Wang, & Menzel, 2023; H. Huang & Huang, 2022), suggesting that longwave radiative sensitivity is mostly determined by the middle and upper tropospheres.

4.3. Theory

The experiments conducted in Section 4.2 suggest that the meridional variations in ϵ can be explained by free-tropospheric temperature lapse rate (Γ_{FT}), troposphere thickness, and surface temperature. These variables are important for longwave radiation and have been used by Feng, Paynter, and Menzel (2023) to explain the radiative feedback parameter under a clear-sky condition. As mentioned above, Feng, Paynter, and Menzel (2023) expects a relatively constant clear-sky ϵ of approximately 0.75. While this is much larger than the all-sky ϵ due to the removal of cloud effects, the magnitude of clear-sky ϵ when a relatively constant Γ_{FT} is maintained in experiment "constant Γ_{FT}" is indeed close to 0.75 (Figure 3). The idealized study cannot explain the weak ϵ in polar climate because, similar to the experiment "constant Γ_{FT}," it assumes no temperature discontinuity between T_s and the atmosphere (Feng, Paynter, & Menzel, 2023; Koll & Cronin, 2018).

The effect of base state T_s on ϵ, assuming independence from atmospheric conditions, can be understood analytically. Denoting the OLR from the surface as $F(T_s)$ and the derivative of $F(T_s)$ with respect to T_s as $F(T_s)'$, if the base state T_s increases by 1 K, the thermal energy passing through the atmosphere increases proportionally by $a = F(T_s)'/F(T_s)$. As a result, the thermal energy absorbed by the WV would increase proportionally to $F(T_s)$ by a, because its absorptivity is independent of T_s. Likewise, the sensitivity of WV radiative effect on specific humidity increases proportionally with T_s by a. Using $F(T_s)$ and $F(T_s)'$ from radiative transfer calculations, we derived the global mean of a as 1.8% K^{-1} (the zonal mean ranges from 1.6 to 2.1% K^{-1}). Alternatively, a can be derived using the surface temperature kernel and $F(T_s)$ estimates from H. Huang and Huang (2022), consistent with ours.

This effect of base state T_s can be incorporated into the analytical formula proposed by Equation 9 of Feng, Paynter, and Menzel (2023) to approximate ϵ as:

$$\epsilon \approx 1 - \frac{\gamma}{1 + \frac{k_{cc} T_{s,FT}}{\frac{g}{R\Gamma} - 1}} + a\mathrm{SFTD} \tag{11}$$

$$\mathrm{SFTD} \equiv T_s - T_{s,FT} = T_s - T_{FT}^m - z_{FT}^m \Gamma_{FT} \tag{12}$$

As defined in Equation 10, $T_{s,FT}$ is the surface temperature assuming a uniform FT lapse rate Γ_{FT} from tropopause to surface under hydrostatic balance. $a = 1.8\%\ K^{-1}$ is derived earlier. Surface and FT temperature differences (surface–free troposphere temperature difference [SFTD]) quantifies the thermal decoupling between the surface and free troposphere, including its thickness. The γ is a fitting parameter that converts the effects on strong WV channels to longwave broadband, as a simplification of Equation 10 of Feng, Paynter, and Menzel (2023), which accounts for the gas overlap and is mainly affected by the relative importance of WV compared to CO_2. Because CO_2 is homogeneous and Section 4.1 has shown that the spatial variation of WV has little effect on ϵ, γ can be assumed as a constant and is empirically derived as 1.8. k_{cc} is the CC scaling at 0.07 K^{-1} (see Equation 5).

The analytical formula (Equation 11) can then be applied to the three experiments conducted in Section 4.2, using the lapse rate and surface temperature of each experiment as input. The results are shown as dotted curves in Figure 3b. For the two experiments with zero SFTD, the analytical formula closely reproduces the small meridional variations in these PRP experiments. Since the two experiments differ only in lapse rates, which the formula captures well, we conclude that higher lapse rates enhance ϵ by increasing thermal emission shift. This conclusion is largely consistent with previous studies on the control of the lapse rate on the thermal emission shift (Feng, Paynter, & Menzel, 2023; Y. Huang & Bani Shahabadi, 2014).

By including the effects of SFTD, the analytical formula explains the meridional variations in ϵ induced by the decoupling of surface temperature from lower-tropospheric temperature (yellow curves with markers in Figure 3b). As visualized in Figures 3f–3h and 4g, SFTD is positive in low latitudes where the lapse rate below the lifting condensation level (LCL) exceeds that above, resulting in enhanced ϵ. In contrast, SFTD becomes negative in regions with near-surface inversions, such as Antarctica, reducing ϵ by up to 0.4. These results demonstrate that SFTD serves as a simple yet effective measure of ϵ under clear-sky conditions.

Building on this insight, we now incorporate the cloud masking effect to explain the full spatial pattern of ϵ, combining the analytical expression for clear-sky ϵ with the cloud masking term approximated by cloud transmittance:

$$\epsilon \approx \left(1 - \frac{\gamma}{1 + \frac{k_{cc} T_{s,FT}}{\frac{g}{R\Gamma} - 1}} + a\mathrm{SFTD} \right) \mathfrak{T}_{\mathrm{cld}}. \tag{13}$$

Figure 4 illustrates how this formulation captures the spatial structure of ϵ. The distribution of clear-sky ϵ (Figures 4a, 4c, and 4e) strongly mirrors that of SFTD. Regions with large positive SFTD, such as the dry subtropical continents with elevated LCLs, exhibit high clear-sky ϵ (red areas in Figures 4b and 4c). These regions often have weak convection, minimal cloud cover, and near-unity transmittance (Figure 4d). As a result, high ϵ persists even under all-sky conditions (Figures 4b and 4f).

10.1029/2025GL115210

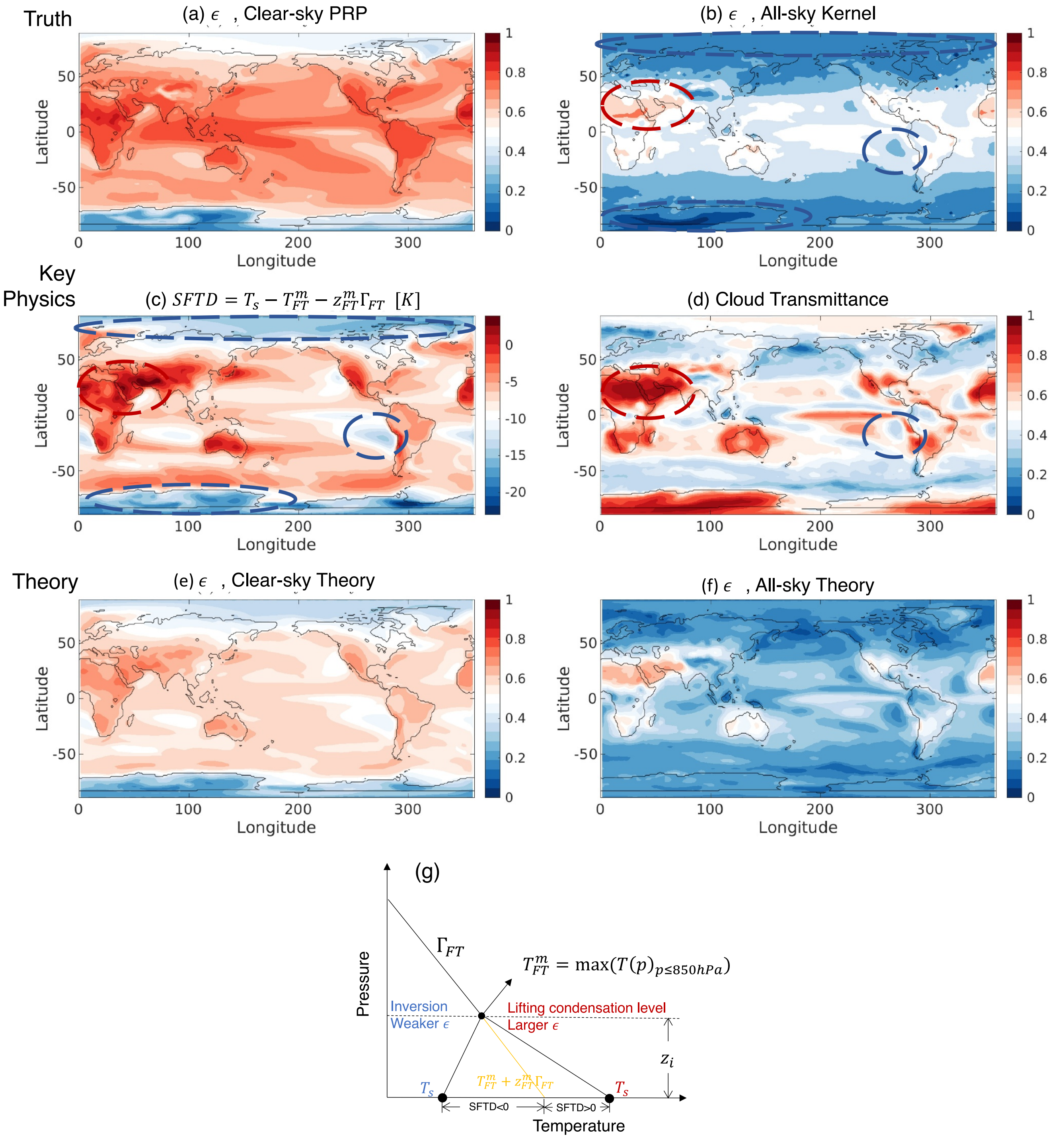

Figure 4. Lower-tropospheric temperature structure controls the efficiency of water vapor. (a) Global distribution of annual mean, multi-model-mean of ϵ based on clear-sky partial radiative perturbation of CMIP6 abrupt 4xCO_2 experiment, following a vertically uniform warming. (b) Is the same as (a), except that the all-sky kernel method (Soden et al., 2008) is applied. (c) Surface and free tropospheric temperature differences (surface–free troposphere temperature difference [SFTD]) derived from the annual mean, multi-model-mean of CMIP6 abrupt 4xCO_2 experiment. (d) Longwave broadband transmittance of clouds ($\mathfrak{T}_{cld}$). (e) Clear-sky ϵ based on Equation 10. (f) All-sky ϵ based on Equation 12. (g) Idealized temperature profile in regions with temperature inversion (linked with negative SFTD, marked as blue) and dry adiabatic lapse rate (linked with positive SFTD, marked as red) in the lower troposphere.

Conversely, regions with near-surface temperature inversions, such as the Arctic, Antarctica, and stratocumulus decks, exhibit negative SFTD and correspondingly low ϵ (blue areas in Figures 4b and 4c). In stratocumulus regions, extensive low-level cloud cover further suppresses ϵ under all-sky conditions (Figures 4b, 4d, and 4f)).

In summary, the spatial variability in longwave radiative efficiency of WV is primarily governed by clear-sky thermodynamic structure, as captured by SFTD, while clouds act as another modulator through their masking effect on thermal radiation.

5. Summary and Discussions

This study introduces a metric to quantify the radiative efficiency of WV (ϵ) in the TOA energy budget (Equation 5). It cleanly isolates the compensating radiative feedback processes caused by warming and moistening under fixed RH (Feng, Paynter, & Menzel, 2023; Held & Shell, 2012; Ingram, 2010, 2013; Jeevanjee et al., 2021; Koll & Cronin, 2018; Koll et al., 2023). The ϵ is found to be nearly model-independent and that the WV feedback is largely a linear function of temperature feedback (Equation 8 and Figures 1b and 1c).

We further show that ϵ exhibits a strong dependence on the climatological base state of temperature and is much weaker at high latitudes than at low latitudes. This state dependency in ϵ is largely attributed to SFTD. We show that local TOA radiative energy is more dominated by temperature changes in regions with negative SFTD (indicating greater inversion strength) and less dominated in regions with positive SFTD (indicating a higher LCL).

Our study emphasizes the importance of the temperature structure in the radiative feedback process. The global mean ϵ is largely controlled by the nearly constant FT lapse rate in the tropical and extratropical regions (Frierson, 2008; Schneider, 2007; Schneider & O'Gorman, 2008). Deviations from the global mean are mainly caused by the near-surface temperature inversion in the high-latitude atmosphere, which is governed by a state of radiative-advective equilibrium (Cronin & Jansen, 2016; Miyawaki et al., 2022; Payne et al., 2015) with influences from sea ice (Boeke et al., 2021; Feldl et al., 2020) and topography (Hahn et al., 2020). It is also important to note that although WV has weak effects on feedback at TOA, it remains crucial through its influence on surface and atmospheric energy budgets (Blanchet et al., 1995; Chung & Feldl, 2024; Curry et al., 1995; Henry et al., 2021).

Data Availability Statement

CMIP6 abrupt 4xCO2 experiment is accessible via https://aims2.llnl.gov/search/cmip6. Radiative kernel data sets are publicly accessible via https://climate.earth.miami.edu/data/radiative-kernels (Soden et al., 2008). Results from partial radiative perturbation experiment are available at Feng (2025).

Acknowledgments
We acknowledge GFDL resources made available for this research. This report was prepared by Jing Feng under award NA23OAR4320198 from the National Oceanic and Atmospheric Administration and U.S. Department of Commerce. The statements, findings, conclusions, and recommendations are those of the author(s) and do not necessarily reflect the views of the National Oceanic and Atmospheric Administration, or the U.S. Department of Commerce. Nadir Jeevanjee and Timothy Merlis are acknowledged for their comments and suggestions on an internal review of the manuscript.

References

Alduchov, O. A., & Eskridge, R. E. (1996). Improved Magnus form approximation of saturation vapor pressure. *Journal of Applied Meteorology and Climatology*, *35*(4), 601–609. https://doi.org/10.1175/1520-0450(1996)035<0601:imfaos>2.0.co;2

Blanchet, J.-P., & Girard, E. (1995). Water vapor-temperature feedback in the formation of continental Arctic air: Its implication for climate. *Science of the Total Environment*, *160*, 793–802. https://doi.org/10.1016/0048-9697(95)04412-t

Boeke, R. C., Taylor, P. C., & Sejas, S. A. (2021). On the nature of the Arctic's positive lapse-rate feedback. *Geophysical Research Letters*, *48*(1), e2020GL091109. https://doi.org/10.1029/2020gl091109

Bony, S., Bellon, G., Klocke, D., Sherwood, S., Fermepin, S., & Denvil, S. (2013). Robust direct effect of carbon dioxide on tropical circulation and regional precipitation. *Nature Geoscience*, *6*(6), 447–451. https://doi.org/10.1038/ngeo1799

Caldwell, P. M., Zelinka, M. D., Taylor, K. E., & Marvel, K. (2016). Quantifying the sources of intermodel spread in equilibrium climate sensitivity. *Journal of Climate*, *29*(2), 513–524. https://doi.org/10.1175/jcli-d-15-0352.1

Charney, J. G., & DeVore, J. G. (1979). Multiple flow equilibria in the atmosphere and blocking. *Journal of the Atmospheric Sciences*, *36*(7), 1205–1216. https://doi.org/10.1175/1520-0469(1979)036<1205:mfeita>2.0.co;2

Chung, P.-C., & Feldl, N. (2024). Sea ice loss, water vapor increases, and their interactions with atmospheric energy transport in driving seasonal polar amplification. *Journal of Climate*, *37*(8), 2713–2725. https://doi.org/10.1175/jcli-d-23-0219.1

Cronin, T. W., & Jansen, M. F. (2016). Analytic radiative-advective equilibrium as a model for high-latitude climate. *Geophysical Research Letters*, *43*(1), 449–457. https://doi.org/10.1002/2015gl067172

Curry, J., Schramm, J., Serreze, M., & Ebert, E. (1995). Water vapor feedback over the Arctic Ocean. *Journal of Geophysical Research*, *100*(D7), 14223–14229. https://doi.org/10.1029/95jd00824

Feldl, N., & Merlis, T. M. (2023). A semi-analytical model for water vapor, temperature, and surface-albedo feedbacks in comprehensive climate models. *Geophysical Research Letters*, *50*(21), e2023GL105796. https://doi.org/10.1029/2023gl105796

Feldl, N., Po-Chedley, S., Singh, H. K., Hay, S., & Kushner, P. J. (2020). Sea ice and atmospheric circulation shape the high-latitude lapse rate feedback. *NPJ Climate and Atmospheric Science*, *3*(1), 41. https://doi.org/10.1038/s41612-020-00146-7

Feng, J. (2025). Radiative feedback parameters of CMIP6 abrupt 4xCO_2 experiment [Dataset]. *Zenodo*. https://doi.org/10.5281/zenodo.14828563

Feng, J., Paynter, D., & Menzel, R. (2023). How a stable greenhouse effect on Earth is maintained under global warming. *Journal of Geophysical Research: Atmospheres*, *128*(9), e2022JD038124. https://doi.org/10.1029/2022jd038124

Feng, J., Paynter, D., Wang, C., & Menzel, R. (2023). How atmospheric humidity drives the outgoing longwave radiation–surface temperature relationship and inter-model spread. *Environmental Research Letters*, *18*(10), 104033. https://doi.org/10.1088/1748-9326/acfb98

Frierson, D. M. (2008). Midlatitude static stability in simple and comprehensive general circulation models. *Journal of the Atmospheric Sciences*, *65*(3), 1049–1062. https://doi.org/10.1175/2007jas2373.1

Hahn, L. C., Armour, K. C., Battisti, D. S., Donohoe, A., Pauling, A., & Bitz, C. M. (2020). Antarctic elevation drives hemispheric asymmetry in polar lapse rate climatology and feedback. *Geophysical Research Letters*, *47*(16), e2020GL088965. https://doi.org/10.1029/2020gl088965

Held, I. M., & Shell, K. M. (2012). Using relative humidity as a state variable in climate feedback analysis. *Journal of Climate*, *25*(8), 2578–2582. https://doi.org/10.1175/jcli-d-11-00721.1

Held, I. M., & Soden, B. J. (2000). Water vapor feedback and global warming. *Annual Review of Energy and the Environment*, *25*(1), 441–475. https://doi.org/10.1146/annurev.energy.25.1.441

Henry, M., Merlis, T. M., Lutsko, N. J., & Rose, B. E. (2021). Decomposing the drivers of polar amplification with a single-column model. *Journal of Climate*, *34*(6), 2355–2365. https://doi.org/10.1175/jcli-d-20-0178.1

Huang, H., & Huang, Y. (2022). A decomposition of the atmospheric and surface contributions to the outgoing longwave radiation. *Journal of Geophysical Research: Atmospheres*, *127*(20), e2022JD036773. https://doi.org/10.1029/2022JD036773

Huang, Y., & Bani Shahabadi, M. (2014). Why logarithmic? A note on the dependence of radiative forcing on gas concentration. *Journal of Geophysical Research: Atmospheres*, *119*(24), 13–683. https://doi.org/10.1002/2014jd022466

Huang, Y., Ramaswamy, V., & Soden, B. (2007). An investigation of the sensitivity of the clear-sky outgoing longwave radiation to atmospheric temperature and water vapor. *Journal of Geophysical Research*, *112*(D5), D05104. https://doi.org/10.1029/2005jd006906

Ingram, W. (2010). A very simple model for the water vapour feedback on climate change. *Quarterly Journal of the Royal Meteorological Society: A Journal of the Atmospheric Sciences, Applied Meteorology and Physical Oceanography*, *136*(646), 30–40. https://doi.org/10.1002/qj.546

Ingram, W. (2013). A new way of quantifying GCM water vapour feedback. *Climate Dynamics*, *40*(3), 913–924. https://doi.org/10.1007/s00382-012-1294-3

Jeevanjee, N., Koll, D. D., & Lutsko, N. (2021). "Simpson's law" and the spectral cancellation of climate feedbacks. *Geophysical Research Letters*, *48*(14), e2021GL093699. https://doi.org/10.1029/2021gl093699

Koll, D. D., & Cronin, T. W. (2018). Earth's outgoing longwave radiation linear due to H_2O greenhouse effect. *Proceedings of the National Academy of Sciences of the United States of America*, *115*(41), 10293–10298. https://doi.org/10.1073/pnas.1809868115

Koll, D. D., Jeevanjee, N., & Lutsko, N. J. (2023). An analytic model for the clear-sky longwave feedback. *Journal of the Atmospheric Sciences*, *80*(8), 1923–1951. https://doi.org/10.1175/jas-d-22-0178.1

Langen, P. L., Graversen, R. G., & Mauritsen, T. (2012). Separation of contributions from radiative feedbacks to polar amplification on an aquaplanet. *Journal of Climate*, *25*(8), 3010–3024. https://doi.org/10.1175/jcli-d-11-00246.1

Manabe, S., & Wetherald, R. T. (1967). Thermal equilibrium of the atmosphere with a given distribution of relative humidity.

Miyawaki, O., Shaw, T. A., & Jansen, M. F. (2022). Quantifying energy balance regimes in the modern climate, their link to lapse rate regimes, and their response to warming. *Journal of Climate*, *35*(3), 1045–1061. https://doi.org/10.1175/jcli-d-21-0440.1

Payne, A. E., Jansen, M. F., & Cronin, T. W. (2015). Conceptual model analysis of the influence of temperature feedbacks on polar amplification. *Geophysical Research Letters*, *42*(21), 9561–9570. https://doi.org/10.1002/2015gl065889

Pithan, F., & Mauritsen, T. (2014). Arctic amplification dominated by temperature feedbacks in contemporary climate models. *Nature Geoscience*, *7*(3), 181–184. https://doi.org/10.1038/ngeo2071

Raghuraman, S. P., Paynter, D., & Ramaswamy, V. (2019). Quantifying the drivers of the clear sky greenhouse effect, 2000–2016. *Journal of Geophysical Research: Atmospheres*, *124*(21), 11354–11371. https://doi.org/10.1029/2019jd031017

Reichler, T., Dameris, M., & Sausen, R. (2003). Determining the tropopause height from gridded data. *Geophysical Research Letters*, *30*(20), 2042. https://doi.org/10.1029/2003gl018240

Schneider, T. (2007). The thermal stratification of the extratropical troposphere. *Sigma: Linguistique Anglaise, Linguistique Generale*, *7*(6), 3.

Schneider, T., & O'Gorman, P. A. (2008). Moist convection and the thermal stratification of the extratropical troposphere. *Journal of the Atmospheric Sciences*, *65*(11), 3571–3583. https://doi.org/10.1175/2008jas2652.1

Shell, K. M., Kiehl, J. T., & Shields, C. A. (2008). Using the radiative kernel technique to calculate climate feedbacks in NCAR's community atmospheric model. *Journal of Climate*, *21*(10), 2269–2282. https://doi.org/10.1175/2007jcli2044.1

Sherwood, S., Webb, M. J., Annan, J. D., Armour, K. C., Forster, P. M., Hargreaves, J. C., et al. (2020). An assessment of Earth's climate sensitivity using multiple lines of evidence. *Reviews of Geophysics*, *58*(4), e2019RG000678. https://doi.org/10.1029/2019rg000678

Smith, C., Nicholls, Z., Armour, K., Collins, W., Forster, P., Meinshausen, M., et al. (2021). The Earth's energy budget, climate feedbacks, and climate sensitivity supplementary material. In V. Masson-Delmotte, et al. (Eds.), *Climate change 2021: The physical science basis. Contribution of working group i to the sixth assessment report of the intergovernmental panel on climate change*. Retrieved from https://www.ipcc.ch/

Soden, B. J., & Held, I. M. (2006). An assessment of climate feedbacks in coupled ocean–atmosphere models. *Journal of Climate*, *19*(14), 3354–3360. https://doi.org/10.1175/jcli3799.1

Soden, B. J., Held, I. M., Colman, R., Shell, K. M., Kiehl, J. T., & Shields, C. A. (2008). Quantifying climate feedbacks using radiative kernels. *Journal of Climate*, *21*(14), 3504–3520. https://doi.org/10.1175/2007jcli2110.1

Taylor, P. C., Cai, M., Hu, A., Meehl, J., Washington, W., & Zhang, G. J. (2013). A decomposition of feedback contributions to polar warming amplification. *Journal of Climate*, *26*(18), 7023–7043. https://doi.org/10.1175/jcli-d-12-00696.1

Wallace, J. M., & Hobbs, P. V. (2006). *Atmospheric science: An introductory survey* (Vol. 92). Elsevier.

Wetherald, R., & Manabe, S. (1988). Cloud feedback processes in a general circulation model. *Journal of the Atmospheric Sciences*, *45*(8), 1397–1416. https://doi.org/10.1175/1520-0469(1988)045<1397:cfpiag>2.0.co;2

Zelinka, M. D., Klein, S. A., & Hartmann, D. L. (2012). Computing and partitioning cloud feedbacks using cloud property histograms. Part I: Cloud radiative kernels. *Journal of Climate*, *25*(11), 3715–3735. https://doi.org/10.1175/jcli-d-11-00248.1

Zelinka, M. D., Myers, T. A., McCoy, D. T., Po-Chedley, S., Caldwell, P. M., Ceppi, P., et al. (2020). Causes of higher climate sensitivity in CMIP6 models. *Geophysical Research Letters*, *47*(1), e2019GL085782. https://doi.org/10.1029/2019gl085782

References From the Supporting Information

Huang, H., & Huang, Y. (2023). Radiative sensitivity quantified by a new set of radiation flux kernels based on the ECMWF reanalysis v5 (ERA5). *Earth System Science Data*, *15*(7), 3001–3021. https://doi.org/10.5194/essd-15-3001-2023

Janoski, T. P., Mitevski, I., Kramer, R. J., Previdi, M., & Polvani, L. M. (2024). Climkern v1. 1.2: A new python package and kernel repository for calculating radiative feedbacks. *EGUsphere*, *2024*, 1–23.

Pincus, R., Mlawer, E. J., & Delamere, J. S. (2019). Balancing accuracy, efficiency, and flexibility in radiation calculations for dynamical models. *Journal of Advances in Modeling Earth Systems*, *11*(10), 3074–3089. https://doi.org/10.1029/2019ms001621